Int. J. Electrochem. Sci., 17 **(2022)** Article Number: 220460, doi: 10.20964/2022.04.60

International Journal of
ELECTROCHEMICAL
SCIENCE
www.electrochemsci.org

Two Different Type Defects in Nano-Structured High Voltage $Li_xNi_{0.5}Mn_{1.5}O_4$(*x* equals to 0.96, 0.98, 1.0, 1.02 and 1.04) with an Fd-3m Space Group

Yu Li[1,2], *Xiang-Bo Shen*[1], *Xiao-Ming Xu*[1], *Chui-Song Zeng*[1], *Wen-Qing Wei*[1], *Yi-Jie Gu*[1,3,*]

[1] School of Mechanical-electronic and Vehicle Engineering, Weifang University, Weifang 261061, China
[2] LiShen Power Battery System Co.LTD, Tianjin 300384, China
[3] College of Materials Science and Engineering, Shandong University of Science and Technology, Qingdao 266510, China
[*]E-mail: guyijie@wfu.edu.cn

Received: 11 December 2021 / *Accepted:* 25 January 2022 / *Published:* 4 March 2022

$Li_xNi_{0.5}Mn_{1.5}O_4$ microspheres (*x* = 0.96, 0.98, 1.0, 1.02, and 1.04), which consist of nanometer-sized primary particles with different lithium contents, were synthesized by an ammonia-mediated carbonate precipitation method. The effects of lithium content on the structure, morphology, and electrochemical characteristics of the prepared microspheres were investigated in detail. Two types of defects in $Li_xNi_{0.5}Mn_{1.5}O_4$, which is in the *Fd*-3*m* space group, were identified: Li vacancies (*x* = 0.96 and 0.98) and Li on Ni sites (*x* = 1.02 and 1.04). X-ray diffraction with Rietveld refinement revealed that approximately 35% of the total manganese in $Li_xNi_{0.5}Mn_{1.5}O_4$ is Mn^{3+}. We suggest that most of the Mn^{3+} did not participate in the reaction during charging and discharging, and the 4.0 V platform of this material cannot be used to accurately estimate the Mn^{3+} content. $Li_{1.0}Ni_{0.5}Mn_{1.5}O_4$, which had no defects, exhibited the best electrochemical performance, retaining a capacity of 146.5 mAh g^{-1} after 10 cycles at 0.1C.

Keywords: $LiNi_{0.5}Mn_{1.5}O_4$, lithium content, Mn^{3+}, cathode materials

1. INTRODUCTION

The conventional approach to increasing the energy storage capacity of a battery is to increase the voltage at the positive electrode [1]. $LiNi_{0.5}Mn_{1.5}O_4$ reportedly has a high discharge platform near 4.7 V and a small platform around 4 V [2–4]. The platform around 4.7 V is assigned to the oxidation–reduction of Ni^{2+}/Ni^{4+}, whereas the 4.0 V platform is attributed to Mn^{3+}/Mn^{4+} oxidation–reduction. Capacity fade in $LiNi_{0.5}Mn_{1.5}O_4$ spinel material has several main causes [5–8]. Among them, the impact

of Mn^{3+} has attracted considerable interest recently [9–11].

The impact of Mn^{3+} defects has been thoroughly examined, but the results are controversial. Capacity fade has also been attributed to the formation of a rock salt impurity phase ($Li_xNi_{1-x}O$) during high-temperature synthesis, which introduces Mn^{3+} ions into the structure. It has been suggested that Mn^{3+} can stabilize the cycling performance and improve the stability [12, 13]. Mn^{3+} causes more Ni and Mn disorder at higher proportions of the *Fd*-3*m* space group and thus increases the Li ion diffusion coefficient and electrical conductivity of $LiNi_{0.5}Mn_{1.5}O_4$. However, it has also been argued that Mn^{3+} ions are more likely to disproportionate by $2Mn^{3+} \rightarrow Mn^{2+} + Mn^{4+}$ [14]. The resulting Mn^{2+} ion is soluble in the electrolyte and can even be electrochemically deposited on the anode, resulting in a significant loss of active substances and capacity during cycling.

Considering the complex internal structure of this material and the difficulty of assessing the interdependence of the structure and electrochemical performance, investigations that focus on the relationship between the structural features and electrochemical properties are expected to promote the application of $LiNi_{0.5}Mn_{1.5}O_4$. In this study, the effects of lithium content on the structure and electrochemical properties of spinel $LiNi_{0.5}Mn_{1.5}O_4$ were investigated. We discuss two types of defects in nanostructured high-voltage $Li_xNi_{0.5}Mn_{1.5}O_4$ (x = 0.96, 0.98, 1.0, 1.02, and 1.04) in the *Fd*-3*m* space group.

2. EXPERIMENTAL

Nickel sulfate hexahydrate ($NiSO_4 \cdot 6H_2O$), manganese sulfate monohydrate ($MnSO_4 \cdot H_2O$), sodium carbonate (Na_2CO_3), and ammonium hydroxide ($NH_3 \cdot H_2O$) were used as the starting materials. A mixed acid solution of $NiSO_4$ and $MnSO_4$ (Ni/Mn = 0.5:1.5, molar ratio) was fed into the reactor at a rate of 0.5 mL/min using a peristaltic pump. A relatively fine needle was used to maintain a droplet volume of 0.01 mL. $NH_3 \cdot H_2O$ (0.3 mol/L) was used as a complexing agent, and Na_2CO_3 (1 mol/L) was used to precipitate the metallic ions. The pH was maintained at approximately 7.8 using a pH meter. Co-precipitation was performed in a 55 °C bath in a continuously stirred tank reactor with stirring at 800 rpm. After 10 h of stirring, the $Ni_{0.5}Mn_{1.5}(CO_3)_2$ precursor was collected and washed four times to remove residual sodium and sulfate radicals; it was then filtered and dried. We thus obtained synthesized $Li_xNi_{0.5}Mn_{1.5}O_4$ samples (x = 0.96, 0.98, 1.0, 1.02, and 1.04). These samples were prepared at 800°C in air.

The structure of the obtained $LiNi_{0.5}Mn_{1.5}O_4$ was characterized by powder X-ray diffraction (XRD, Rigaku D/Max2500PC, Japan) using CuKα radiation, a graphite monochromator, a tube voltage of 30 kV, a tube current of 100 mA, and a step size of 0.02° from 10° to 120°. A gas displacement pycnometer using He gas (3H-2000TD, China) was used to measure the true density of the samples. The morphology and microstructure of the samples were studied using field emission scanning electron microscopy (SEM, FEI, Nova Nano SEM450, USA). For all electrochemical measurements, the synthesized cathode materials were used in CR2016 coin cells with a metallic lithium plate as the counter electrode. The as-synthesized $LiNi_{0.5}Mn_{1.5}O_4$, carbon black, and polyvinylidene fluoride were mixed at a weight ratio of 8:1:1 in *N*-methyl-2-pyrrolidone to form a slurry. The slurry was coated on aluminum

foil and then dried in a vacuum oven at 120 °C for 12 h. The electrolyte was a 1 M $LiPF_6$ solution in ethylene carbonate/dimethyl carbonate/ethyl methyl carbonate in a 1:1:1 volume ratio. A Cellgard 2400 membrane was used as the electrode separator. Charge/discharge tests were performed in a voltage range of 3.5–4.9 V using a battery test system (LAND-CT2001A, China). Electrochemical impedance spectroscopy (EIS) was performed using an impedance analyzer (Zahner Elektrik IM6, Germany) in a frequency range of 100 mHz to 100 kHz at an amplitude of 10 mV.

3. RESULTS AND DISCUSSION

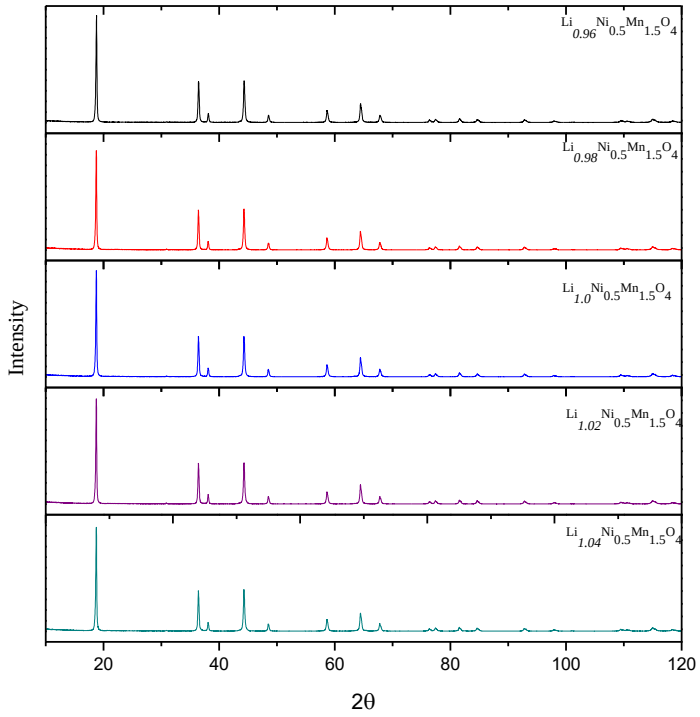

Figure 1. XRD patterns of $Li_xNi_{0.5}Mn_{1.5}O_4$ samples (x = 0.96, 0.98, 1.0, 1.02, and 1.04).

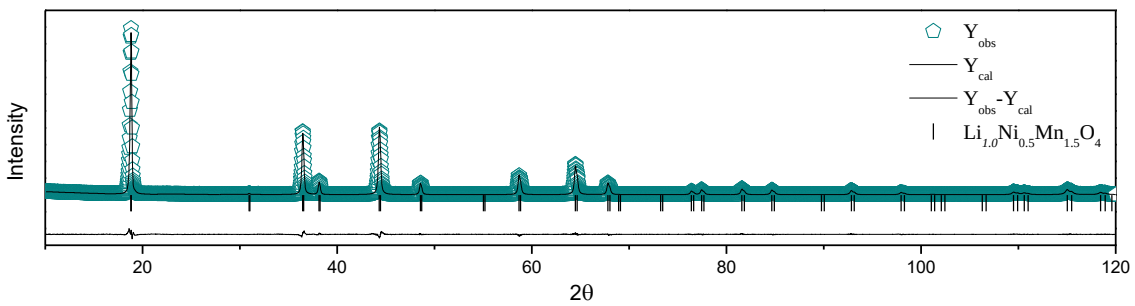

Figure 2. Comparison of experimental and calculated XRD patterns of $Li_{1.0}Ni_{0.5}$ $Mn_{1.5}O_4$.

Figure 1 shows the XRD patterns of $Li_xNi_{0.5}Mn_{1.5}O_4$ (x = 0.96, 0.98, 1.0, 1.02, and 1.04). To further understand the structure of $Li_xNi_{0.5}Mn_{1.5}O_4$, all the XRD data were refined, and the XRD patterns are compared with the refined patterns in Figure 2. Table 1 presents the structural parameters of the materials based on the refinement of the XRD data. The XRD patterns in Figure 1 correspond to diffraction from the typical face-centered cubic spinel structure (space group *Fd*-3*m*) irrespective of Li content. No additional diffraction peaks associated with secondary phases were observed. As shown in Table 1, the XRD data are fitted by a strict three-dimensional model, $\{LiNi_x\}_{8a}\{Ni_{0.5}[Mn^{4+}]_{1.5-y}[Mn^{3+}]_y\}_{16d}\{O_w\}_{32e}$. The B_{iso} values of $Li_{0.96}Ni_{0.5}Mn_{1.5}O_4$ and $Li_{0.98}Ni_{0.5}Mn_{1.5}O_4$ indicate that there are traces of Li vacancies for x = 0.96 and 0.98. The structure of $Li_{0.96}Ni_{0.5}Mn_{1.5}O_4$ can be described as $\{Li_{0.960}Ni_{0.0228}\}_{8a}\{Ni_{0.5}[Mn^{4+}]_{1.124}[Mn^{3+}]_{0.376}\}_{16d}\{O_{3.792}\}_{32e}$. For x = 0.98 and 1.0, the structure may be represented as $\{Li_{0.98}$ $Ni0.0156\}_{8a}\{Ni_{0.5}[Mn^{4+}]_{1.12}[Mn^{3+}]_{0.38}\}_{16d}\{O_{3.8}\}_{32e}$ and $\{Li\}_{8a}\{Ni_{0.5}[Mn^{4+}]_{1.052}[Mn^{3+}]_{0.448}\}_{16d}\{O_{3.766}\}_{32e}$, respectively. When the Li content exceeds 1.0, Li occupies Ni sites. The occupation of the 16d site by Li^+ ions is found to be 0.01 and 0.02 in $Li_{1.02}Ni_{0.5}Mn_{1.5}O_4$ and $Li_{1.04}Ni_{0.5}Mn_{1.5}O_4$, respectively. That is, there are two types of defects in nanostructured high-voltage $Li_xNi_{0.5}Mn_{1.5}O_4$ (x = 0.96, 0.98, 1.0, 1.02, and 1.04) in the *Fd*-3*m* space group: Li vacancies (x = 0.96 and 0.98) and Li on Ni sites (x = 1.02 and 1.04). The measured and calculated densities of $Li_{1.02}Ni_{0.5}Mn_{1.5}O_4$ were 4.3648 and 4.4599 g cm^{-3}, respectively. This result strongly indicates the presence of oxygen vacancies. The structure of $Li_xNi_{0.5}Mn_{1.5}O_4$ may also be expressed as $0.5LiNiMnO_{3.5}\cdot0.5Li[Mn^{4+}]_{2-\delta}[Mn^{3+}]_\delta O_4$. First-principle calculations have shown that strong interactions between Ni^{2+} and Mn^{4+} ions are favored [15]. Therefore, in the model $0.5LiNiMnO_{3.5}\cdot0.5Li[Mn^{4+}]_{2-\delta}[Mn^{3+}]_\delta O_4$, the presence of Ni and Mn in a 1:1 ratio is relatively easy to understand, and it is also consistent with the formation of Ni^{2+} and Mn^{4+} clusters within the transition metal layers [16]. In $LiMn_2O_4$, the valence of Mn is reportedly 3.5; that is, Mn^{4+}/Mn^{3+} = 1:1.

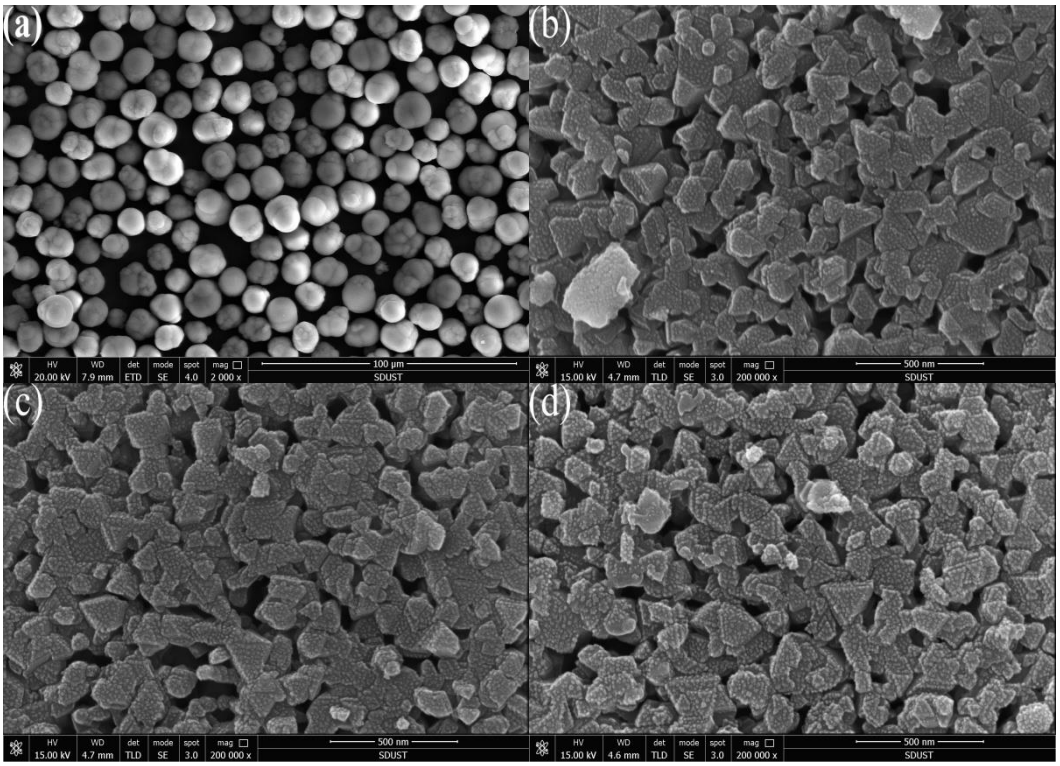

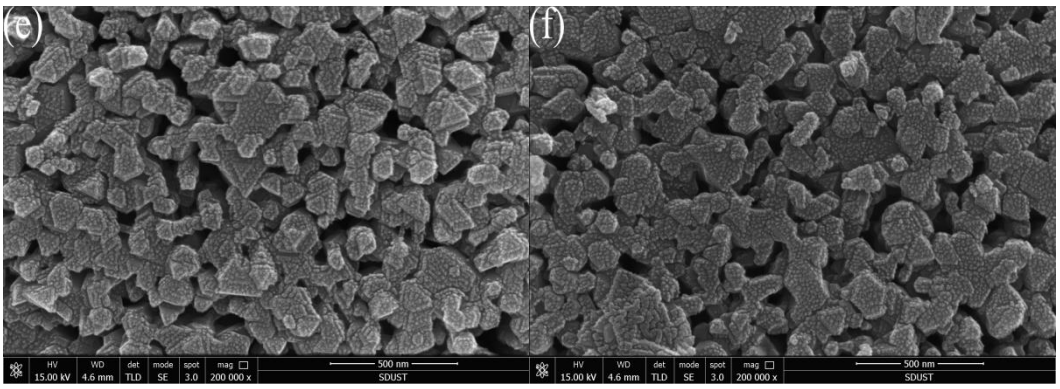

Figure 3. SEM images of (a) precursor under low magnification showing single particle size and distribution and synthesized $Li_xNi_{0.5}Mn_{1.5}O_4$ samples under high magnification for x = 0.96 (b), 0.98 (c), 1.0 (d), 1.02 (e), and 1.04 (f).

Figure 3 shows SEM images of the $Ni_{0.5}Mn_{1.5}(CO_3)_2$ precursor and the obtained $Li_xNi_{0.5}Mn_{1.5}O_4$ (x = 0.96, 0.98, 1.0, 1.02, and 1.04) samples. As shown in Figure 3(a), the precursor has clear spherical morphology with a uniform size distribution, and its diameter is approximately 10 μm. The precursor powder is homogeneous, and the particles are not agglomerated. The spherical morphology and diameter in the $Li_xNi_{0.5}Mn_{1.5}O_4$ samples was unchanged after high-temperature calcination. To examine the microstructure of the $Li_xNi_{0.5}Mn_{1.5}O_4$ samples, Figure 3(b)–3(f) show the surface morphology of a single particle of each sample at high magnification. The five samples have similar particle morphology, with no substantial differences. Both of samples were composed of many octahedral primary particles with sizes of 50–300 nm, which will enhance the electrochemical performance by decreasing the lithium ion diffusion length [17–19] and increasing the effective surface contact area with the electrolyte.

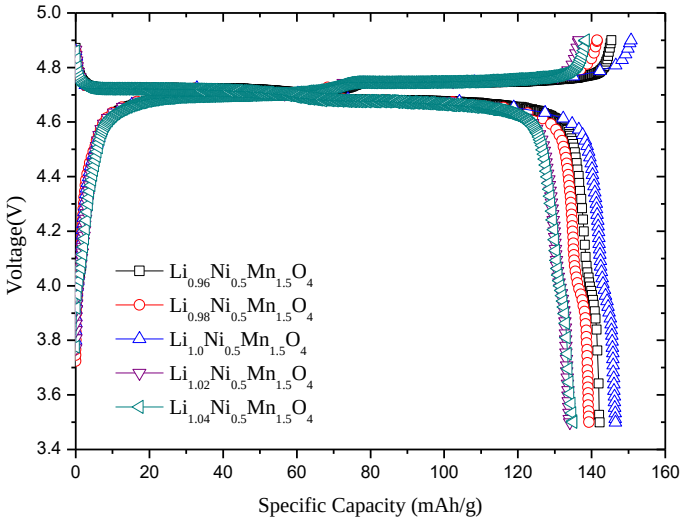

Figure 4. Tenth charge/discharge curves of $Li_xNi_{0.5}Mn_{1.5}O_4$ (x = 0.96, 0.98, 1.0, 1.02, and 1.04) tested against a Li metal anode at a rate of 0.1C between 3.5 and 4.9 V.

Charge/discharge tests were conducted at a rate of 0.1C from 3.5 to 4.9 V, and the 10th charge/discharge curves are shown in Figure 4. The $Li_{1.0}Ni_{0.5}Mn_{1.5}O_4$ sample had the highest discharge

capacity of 146.5 mAh g^{-1}. The samples with x = 0.96, 0.98, 1.02, and 1.04 had discharge capacities of 142.2, 139.3, 134.1, and 135 mAh g^{-1}, respectively; these values are all lower than that of $Li_{1.0}Ni_{0.5}Mn_{1.5}O_4$. The reason may be the presence of Li vacancies (x = 0.96 and 0.98) and the occupation of Ni sites by Li (x = 1.02 and 1.04). We suggest that not all of the Mn^{3+} participates in the reaction during charging and discharging. As clearly shown in Figure 4, all the cathodes exhibited two typical plateaus: a distinct long, flat plateau around 4.7 V, which is attributed to the $Ni^{2+/4+}$ redox reaction, and a short plateau around 4.0 V resulting from the $Mn^{3+/4+}$ redox process. The length of the plateau in the 4.0 V region can be adopted to calculate the relative Mn^{3+} content of the spinels [20]. Therefore, a detailed analysis was performed to calculate the capacity contribution of Mn^{3+} in all the samples from the discharge capacity of the 5th cycle; the results are presented in Table 2. The capacity of the 4.0 V plateau (which is calculated to lie between 3.5 and 4.2 V) is 4.3, 4.4, 4.6, 4.2, and 5.2 mAh g^{-1} for x = 0.96, 0.98, 1.0, 1.02, and 1.04, respectively. Interestingly, the percentage of the capacity at the 4.0 V plateau is approximately 3%, but the Mn^{3+} content observed by XRD refinement is approximately 20–50%. We suggest that most of the Mn^{3+} was not oxidized/reduced during charging/discharging, and the capacity of the 4.0 V platform cannot be used to accurately estimate the Mn^{3+} content.

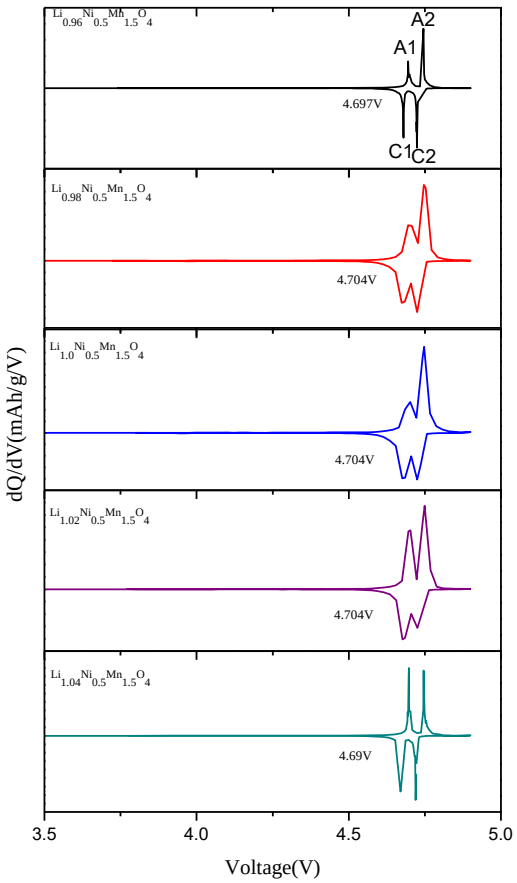

Figure 5. Differential capacity versus voltage curves of Li/$Li_xNi_{0.5}Mn_{1.5}O_4$ (x = 0.96, 0.98, 1.0, 1.02, and 1.04) cell between 3.5 and 4.9 V at a rate of 0.1C.

Figure 5 shows that the two reduction peaks are divided by a voltage point (*Q*) corresponding to the biggest d*Q*/d*V* value between the two peaks during discharge, and these voltage limits clearly separate the voltage plateaus. We use the discharge capacity in the voltage ranges of 4.3 V–*Q* and *Q*–4.9 V to represent the transition from the second cubic phase to the pristine cubic phase and the transition from the third cubic phase to the second cubic phase, respectively [21].

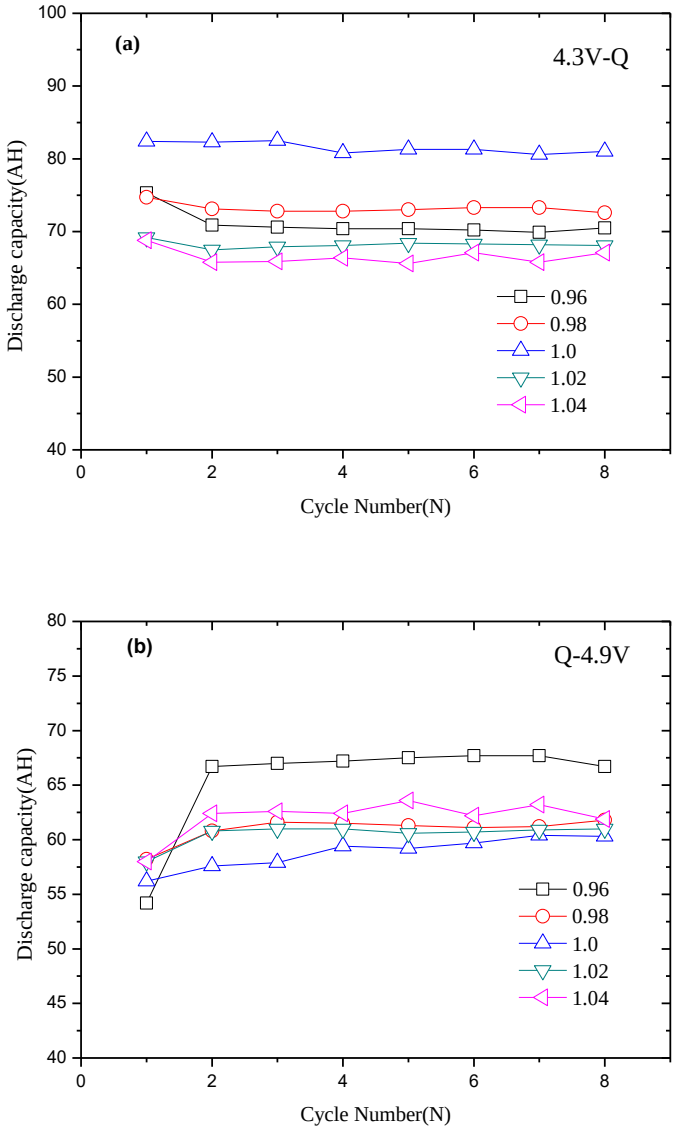

Figure 6. (a) Discharge capacity versus cycle number during Li^+ intercalation for $Li_xNi_{0.5}Mn_{1.5}O_4$ (x = 0.96, 0.98, 1.0, 1.02, and 1.04) tested against a Li metal anode at a rate of 0.1C (a) between 4.3 V and *Q* and (b) between *Q* and 4.9 V.

Figure 6 shows plots of discharge capacity versus Li content for $Li_xNi_{0.5}Mn_{1.5}O_4$ (x = 0.96, 0.98, 1.0, 1.02, and 1.04) during Li^+ intercalation with a Li metal anode at a rate of 0.1C in the voltage ranges of 4.3 V–*Q* and *Q*–4.9 V. In the discharge process, we chose 4.9 and 4.3 V as the cutoff voltages and used the discharge capacity in the voltage ranges of 4.3 V–*Q* and *Q*–4.9 V to indicate phase transitions. The discharge capacity at 4.3 V–*Q* for samples with both types of defects [Li vacancies (x = 0.96 and

0.98) and Li on Ni sites (x = 1.02 and 1.04)] is lower than that of $Li_{1.0}Ni_{0.5}Mn_{1.5}O_4$. In addition, for samples with both types of defects, the discharge capacity at Q–4.9V is higher than that of $Li_{1.0}Ni_{0.5}Mn_{1.5}O_4$. The reason may be that the transition from the second cubic phase to the pristine cubic phase occurs most rapidly and the transition from the third cubic phase to the second cubic phase occurs most slowly in $Li_{1.0}Ni_{0.5}Mn_{1.5}O_4$. The overall discharge capacity depends largely on the discharge capacity in the voltage range of 4.3 V–Q.

All the samples have two redox peaks near 4.7 V, in agreement with the charge/discharge curves. The difference (ΔV) or polarization between the anodic (A1 and A2) and cathodic (C1 and C2) peaks can be used to estimate how easily Li^+ ion insertion/extraction occurs [22]. Table 3 lists the potential differences between the anodic and cathodic peaks of the five cathodes at ~4.7 V. All five cathodes clearly show small potential differences. For the samples with x = 0.96 and 1.04, the potential differences are slightly larger than those of the samples with x = 0.98, 1.0, and 1.02, implying lower conductivity among them. $Li_{1.0}Ni_{0.5}Mn_{1.5}O_4$, which has the best electrochemical performance, has the smallest potential difference.

Table 1. Structural parameters of $Li_xNi_{0.5}Mn_{1.5}O_4$ samples (x = 0.96, 0.98, 1.0, 1.02, and 1.04).

Samples		$Li_{0.96}Ni_{0.5}Mn_{1.5}O_4$	$Li_{0.98}Ni_{0.5}Mn_{1.5}O_4$	$Li_{1.0}Ni_{0.5}Mn_{1.5}O_4$	$Li_{1.02}Ni_{0.5}Mn_{1.5}O_4$	$Li_{1.04}Ni_{0.5}Mn_{1.5}O_4$
Space group		Fd-3m	Fd-3m	Fd-3m	Fd-3m	Fd-3m
				Lattice constant		
a(Å)		8.16824	8.1693	8.1691	8.1699	8.1698
Cell volume(Å ^{3})		544.987	545.198	545.156	545.318	545.303
				Structure parameters		
R_p		6.27	6.07	6.29	7.9	6.66
R_{wp}		9.9	9.62	9.72	11	10.3
Li_{8a}	x	0.12500	0.12500	0.12500	0.12500	0.12500
	y	0.12500	0.12500	0.12500	0.12500	0.12500
	z	0.12500	0.12500	0.12500	0.12500	0.12500
	Occ	0.96	0.98	1	1	1
	B_{iso}	1.795	1.235	1.0	1.2	1.913
Ni_{16d}	x	0.50000	0.50000	0.50000	0.50000	0.50000
	y	0.50000	0.50000	0.50000	0.50000	0.50000
	z	0.50000	0.50000	0.50000	0.50000	0.50000
	Occ	0.2386	0.2422	0.25	0.2475	0.245
	B_{iso}	0.073	0.137	0.409	0.442	0.504
Mn_{16d}	x	0.50000	0.50000	0.50000	0.50000	0.50000
	y	0.50000	0.50000	0.50000	0.50000	0.50000
	z	0.50000	0.50000	0.50000	0.50000	0.50000
	Occ	0.75	0.75	0.75	0.7425	0.735
	Biso	0.073	0.137	0.409	0.442	0.504
Ni_{8a}	x	0.125	0.125			
	y	0.125	0.125			
	z	0.125	0.125			

	Occ	0.0228	0.0156			
	B_{iso}	1.795	1.235			
Li_{16d}	x	-	-	-	0.50000	0.50000
	y	-	-	-	0.50000	0.50000
	z	-	-	-	0.50000	0.50000
	Occ	-	-	-	0.01	0.02
	B_{iso}	-	-	-	0.442	0.504
O_{32e}	x	0.26190	0.26211	0.26358	0.26015	0.26360
	y	0.26190	0.26211	0.26358	0.26015	0.26360
	z	0.26190	0.26211	0.26358	0.26015	0.26360
	Occ	0.948	0.95	0.944	0.907	0.9058
	B_{iso}	0.392	0.391	0.34	0.304	0.6447

Table 2. Values and percentages of Mn^{3+} content and 4.0 V plateau capacity.

Li content	4.0V plateau capacity(mAh g^{-1}) (3.5-4.2V)	The percentage of 4.0V plateau capacity (%)	Mn^{3+} amount	The percentage of Mn^{3+} amount (%)
0.96	4.3	3.02	0.376	25.07
0.98	4.4	3.16	0.38	25.33
1.0	4.6	3.14	0.448	29.87
1.02	4.2	3.13	0.754	50.27
1.04	5.2	3.85	0.7536	50.24

Table 3. Potential difference between anodic peak (A1/A2) and cathodic peak (C1/C2) of each sample.

samples	0.96	0.98	1.0	1.02	1.04
Potential difference A1-C1(mV)	31.5	20	20	19.3	28
Potential difference A2-C2(mV)	44	44	44	44	49

To study the change in impedance of the $Li_xNi_{0.5}Mn_{1.5}O_4$ (x = 0.96, 0.98, 1.0, 1.02, and 1.04) cathodes, EIS was performed. Figure 7 presents the Nyquist plots of the spinel electrodes after cycling at 0.1C. All the EIS spectra contain one semicircle in the high- and medium-frequency regions and an inclined line in the low-frequency zone. The charge-transfer resistance R_{ct}, which is roughly the radius of the semicircle, was simulated. The $Li_{1.0}Ni_{0.5}Mn_{1.5}O_4$ cathode has a smaller charge-transfer impedance (178.4 Ω) than the other four samples.

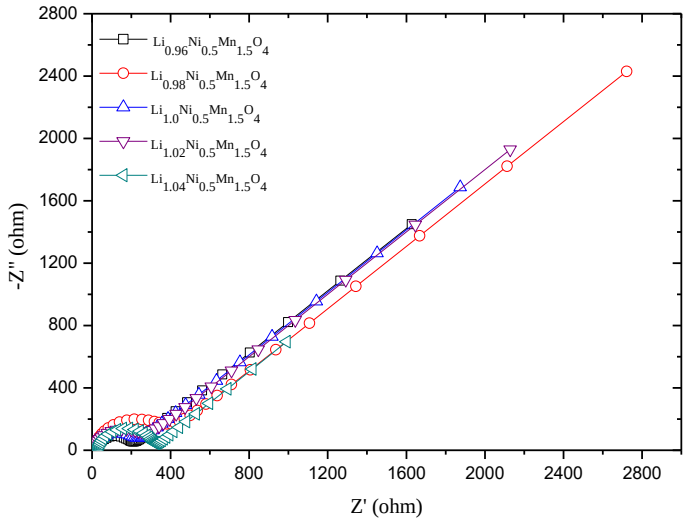

Figure 7. Nyquist plots of synthesized $Li_xNi_{0.5}Mn_{1.5}O_4$ (x = 0.96, 0.98, 1.0, 1.02, and 1.04) cathodes at a rate of 0.1C after 10 cycles between 3.5 and 4.9V.

4. CONCLUSIONS

This work discussed the effects of lithium content on the structure, morphology, and electrochemical characteristics of $Li_xNi_{0.5}Mn_{1.5}O_4$ (x = 0.96, 0.98, 1.0, 1.02, and 1.04) in the *Fd*-3*m* space group. There are two types of defects in the nanostructured high-voltage $Li_xNi_{0.5}Mn_{1.5}O_4$ (x = 0.96, 0.98, 1.0, 1.02, and 1.04): Li vacancies (x = 0.96 and 0.98) and Li on Ni sites (x = 1.02 and 1.04). In the presence of lithium defects, nickel occupies the lithium site, and there is a vacancy at the lithium site. We found that only a small portion of the Mn^{3+} was involved in the electrochemical reaction during charge/discharge, and most of the remaining Mn^{3+} did not participate in the reaction. Among all the materials, $Li_{1.0}Ni_{0.5}Mn_{1.5}O_4$ exhibited the best electrochemical performance, retaining a capacity of 146.5 mAh g^{-1} after 10 cycles at 0.1 C, because it had the smallest potential difference between the anodic and cathodic peaks at ~4.7 V.

ACKNOWLEDGEMENTS
This work was financially supported by National Natural Science Foundation of China (No. 51202131), Postdoctoral Science Foundation of China (2013M541907), Shandong Province Natural Science Foundation (Grant No. ZR2012EMQ002) and Special funds for independent innovation and transformation of achievements in Shandong Province (Grant No. 2014CGZH0911)

References

1. J. Cabana, M. Casas-Cabanas, F. O. Omenya, N. A. Chernova, D. Zeng, M. S. Whittingham and C. P. Grey, *Chem. Mater.*, 24 (2012) 2952.
2. G. Q. Liu, L. Wen and Y. M. Liu, *J. Solid State Electrochem.*, 14(2010) 2191.

3. R. Santhanam and B. Rambabu, *J. Power Sources,* 195 (2010) 5442.
4. X.H. Ma, B. Kang and G. Ceder, *J. Electrochem. Soc*., 157 (2010) A925.
5. A. Manthiram, K. Chemelewski and E. Lee, *Energy Environ. Sci.,* 7 (2014) 1339.
6. N. P. W. Pieczonka, Z. Liu, Peng Lu, K. L. Olson, J. Moote, B. R. Powell and J. Kim, *J. Phys. Chem. C,* 117 (2013), 15947.
7. J. H. Kim, A. Huq, M. Chi, N. P. W. Pieczonka, E. Lee, C. A. Bridges, M. M. Tessema, A. Manthiram, K. A. Persson and B. R. Powell, *Chem. Mater*., 26 (2014) 4377.
8. J. Song, D. W. Shin, Y. H. Lu, C. D. Amos, A. Manthiram and J. B. Goodenough, *Chem. Mater*., 24 (2012) 3101.
9. Y. Qian, Y. Deng, L.Wan, H. Xu, X. Qin and G. Chen, *J. Phys. Chem. C,* 118 (2014) 15581.
10. Yu-Feng Deng, Shi-Xi Zhao, Peng-Yuan Zhai, Guozhong Cao and Ce-Wen Nan, *J. Mater. Chem*. A, 3 (2015) 20103.
11. Y. X. Qian, Y. F. Deng, L. N. Wan, X. S. Qin and G. H. Chen, *J. Phys. Chem*. C, 118 (2014) 15581.
12. G. Q. Wang, J. Xie, C. Y. Wu, S. C. Zhang, G. S. Cao and X. B. Zhao, *J. Power Sources,* 265 (2014) 118.
13. S. Brutti, G. Greco, P. Reale and S. Panero, *Electrochim. Acta*, 106 (2013) 483.
14. Y.S. Meng, G. Ceder, C.P. Grey, W.S. Yoon and Y. Shao-Horn, *Electrochem. Solid State* Lett., 7 (2004) A155.
15. D. Zeng, J. Cabana, J. Bréger, W.S. Yoon and C.P. Grey, *Chem. Mater*., 19 (2007) 6277.
16. N. D. Rosedhi, N. H. Idris, M. M. Rahman, M.F. MdDin and J. Wang, *Electrochimica Acta*, 206, (2016), 374.
17. Ting-Feng Yi, Zi-Kui Fang, Ying Xie, Yan-Rong Zhu and Li-Ya Zang, *Electrochimica Acta*, 147, (2014), 250.
18. X. Zhang, F. Cheng and J. Yang, *Nano Lett*., 13(2013) 2822.
19. Y. Deng, S. Zhao, P. Zhai, G. Cao and C. Nan*, J. Mater. Chem*. A, 3 (2015) 20103.
20. Yi-Jie Gu, Yu Li, Yun-Bo Chen and Hong-Quan Liu, *Electrochimica Acta,* 213(2016) 368.
21. J. Gao, J. Li, C. Jiang and C. Wan, *J. Electrochem. Soc*., 157 (2010) A899.